



**HAL**  
open science

# On the superionic transition in uranium dioxide: Insights from molecular dynamics and lattice dynamics simulations

Paul Fossati, Patrick A. Burr, Michael W. D. Cooper, Conor O. T. Galvin,  
Robin W. Grimes

► **To cite this version:**

Paul Fossati, Patrick A. Burr, Michael W. D. Cooper, Conor O. T. Galvin, Robin W. Grimes. On the superionic transition in uranium dioxide: Insights from molecular dynamics and lattice dynamics simulations. *Physical Review Materials*, 2024, 8, pp.115404. 10.1103/PhysRevMaterials.8.115404 . cea-04926123

**HAL Id: cea-04926123**

**<https://cea.hal.science/cea-04926123v1>**

Submitted on 3 Feb 2025

**HAL** is a multi-disciplinary open access archive for the deposit and dissemination of scientific research documents, whether they are published or not. The documents may come from teaching and research institutions in France or abroad, or from public or private research centers.

L'archive ouverte pluridisciplinaire **HAL**, est destinée au dépôt et à la diffusion de documents scientifiques de niveau recherche, publiés ou non, émanant des établissements d'enseignement et de recherche français ou étrangers, des laboratoires publics ou privés.

# On the superionic transition in uranium dioxide — Insights from molecular dynamics and lattice dynamics simulations

Paul C. M. Fossati,<sup>1,\*</sup> Patrick A. Burr,<sup>2</sup> Michael W. D. Cooper,<sup>3</sup> Conor O. T. Galvin,<sup>3</sup> and Robin W. Grimes<sup>4</sup>

<sup>1</sup>*Université Paris-Saclay, CEA, Service de Recherche en Corrosion et Comportement des Matériaux, 91190, Gif-sur-Yvette, France*

<sup>2</sup>*School of Mechanical and Manufacturing Engineering,*

*University of New South Wales, Kensington, 2052, NSW, Australia*

<sup>3</sup>*Materials Science and Technology Division, Los Alamos National Laboratory, P.O. Box 1663, Los Alamos, NM, 87545, USA*

<sup>4</sup>*Department of Materials, Imperial College London, London, SW7 2AZ, UK*

(Dated: October 2024)

**This is the accepted manuscript of the article published in *Phys. Rev. Mater.* **8**, 115404 (2024), <https://doi.org/10.1103/PhysRevMaterials.8.115404>.**

This study employs molecular dynamics (MD) simulations and lattice dynamics (LD) calculations to investigate the superionic transition in  $\text{UO}_2$ , as well as the characteristics of the superionic phase. The superionic transition is found to be a second-order phase transition associated with an inflection point in enthalpy and lattice parameter at 2600 K. This resembles displacive phase transitions and is associated with an oxygen vibration mode becoming imaginary. The superionic state shows a combination of different local environments and dynamic features similar to glass-forming liquids. The analysis of its dynamics reveals seemingly contradictory characteristics: properties follow those of the lower-temperature crystalline phase in some respects, while exhibiting liquid-like behavior in others. The study highlights the complexity of the superionic phase, including heterogeneous mobility and diffusion mechanisms involving string-like anion clusters.

## I. INTRODUCTION

Accurate knowledge of the thermophysical behavior of uranium dioxide ( $\text{UO}_2$ ) is crucial for optimizing its use as a nuclear fuel. A comprehensive understanding of high-temperature properties is also essential for assessing fuel behavior in accident conditions. This has led to a considerable number of experimental and numerical studies being carried out over the years and summarized in extensive reviews [1–3]. However, conflicting observations of some key properties persist, especially at temperatures close to its melting point. The topic of the superionic transition is a particular example. The existence of a phase transition in solid  $\text{UO}_2$  at temperatures around 80% of its melting point has been known since the late 1960s and early 1970s. It was first described by Dworkin and Bredig [4] in different materials, and called the *diffuse transition*. It was called the Bredig transition,  $\Lambda$  transition, or pre-melting by various authors, because the heat capacity peak occurs at  $T_{\zeta} \sim 85\%$  of the melting temperature  $T_m$ , or around 2670 K [5, 6]. The melting point of  $\text{UO}_2$  is in the range 3030 K–3300 K, with most values close to 3100 K [2]. The transition is also more descriptively called the superionic transition, because of the oxygen ionic superconducting character of the phase [7].

This transition was hypothesized in  $\text{UO}_2$  by Leibowitz *et al.* in 1968 [8], based on the analysis of enthalpy increment measurements at high temperature, and then demonstrated by Bredig in 1972 [5]. It is characterized by a sharp  $\Lambda$ -shaped peak in the heat capacity [5, 6, 9–11],

or equivalently by a small contribution to the enthalpy increment [8]. An inflection point similar to the enthalpy increment has been reported for the lattice parameter using empirical potentials, resulting in another peak observed in the linear thermal expansion coefficient with a maximum in the range 2300 K–3500 K, depending on the potential [12, 13]. The cause of the superionic transition remains controversial in the literature. Some authors ascribe it to the accumulation of point defects [7, 14], while others discuss it in terms of a time-scale change of collective relaxation mechanisms [15]. Likewise, the structure of  $\text{UO}_2$  in the superionic phase is debated, and is sometimes described as a highly-defective solid, or as the combination of a liquid-like oxygen sublattice and a still-crystalline cation sublattice [16, 17]. Previous works showed structural changes, with the appearance of local environments similar to the *Pbcn* structure in the superionic phase [18]. Despite these disagreements, the existence itself of the superionic transition has been demonstrated several times, and has been the focus of numerous studies in recent years. This transition has been reproduced in the literature using atomic-scale models based on several different empirical potentials for  $\text{UO}_2$  [12–14, 16, 19], but also for  $\text{PuO}_2$  [20, 21]. It was documented in several mixed oxides, both stoichiometric and hypostoichiometric [19–27]. Although most of these studies were based on empirical potentials, the transition was also reproduced in DFT simulations [26]. Previous works indicate that this transition is likely to occur in all compounds with the fluorite structure [18], such as  $\text{CaF}_2$  [28],  $\text{Li}_2\text{O}$  [29], and  $\text{CeO}_2$  [30]. The associated structural disorder has been linked with the freezing of some low-energy optical (LEO) vibration modes [31], but also with the energy of formation of Frenkel defects [7].

---

\* paul.fossati@cea.fr

Compounds with other structures can also undergo a similar type of transition when they exhibit a chemical bond hierarchy, with some bonds much weaker than others [32].

In addition to the superionic transition, an unexpected increase of the enthalpy increment was observed. The onset of this anomalous heat has been measured in the range 1 600 K–2 200 K [33]. It is commonly attributed to anharmonic phenomena [34], including the formation of oxygen Frenkel pairs (OFP) [11, 35], although the role of electronic defects was also considered [36–38]. Experiments to quantify oxygen disorder confirmed a significant increase in oxygen defects starting at around 2 000 K, in line with the onset of the anomalous increase in heat capacity at high temperatures [39, 40]. Since then, other experiments have confirmed that, although electronic defects contribute to the increase of the heat capacity, oxygen Frenkel disorder was the major contribution to the superionic transition itself [11].

The purpose of the present study is to provide a consistent framework to better explain and understand the superionic transition in  $\text{UO}_2$ , particularly from a dynamics point of view, supported by atomic-scale simulations. The role of OFP and the effect of vibration modes will be investigated, as well as the dynamical structure of the superionic phase. This emphasis on dynamic features complements previous works focused on structural aspects of this transition [18].

## II. METHODS

The simulations presented in this article are based on semi-empirical potentials using pairwise and many-body interactions. Two types of simulations have been carried out, to investigate two different aspects of the superionic transition: molecular dynamics (MD) and lattice dynamics (LD).

### 1. Empirical potential

The potential model used throughout this study is that of Cooper–Rushton–Grimes (CRG) [20, 41]. This potential has been shown to reproduce the high-temperature thermophysical properties of  $\text{UO}_2$ , as well as other actinide single oxides [20] and mixed oxides [42], including the superionic transition. It also predicts the correct temperature for the melting point of  $\text{UO}_2$  and mixed oxides [22, 43]. Thus, whilst some systematic shift is expected for some properties because of the empirical character of the model, trends and the evolution of the material’s properties are accurately reproduced.

The CRG model is based on rigid ions with partial charges, with a combination of pair interactions and many-body EAM contributions. The electrostatic contribution to the energies and forces are modelled using the Wolf summation technique [44] to transform long-range

electrostatic interactions in a short-range potential, using a convergence factor of  $0.3 \text{ \AA}^{-1}$ .

### 2. Molecular dynamics

MD simulations were carried out using the LAMMPS code [45]. This program has the advantage of offering high-quality implementations of the Nosé–Hoover thermostat and Parinello–Rahman barostat in its Tuckerman integrator [46]. All the simulations used a timestep of 0.002 ps, and characteristic relaxation times of 0.01 ps and 1.0 ps for the barostats and thermostats respectively. Equilibrium MD calculations were performed at several temperatures across the 300 K–4 000 K range, with a temperature interval of 46,25 K. The initial structure of the simulation boxes consisted in  $12 \times 12 \times 12$  supercells of the perfect  $Fm\bar{3}m$  structure. This corresponds to lengths of 65 Å and 20 736 atoms. Each simulation consists of a fixed-temperature and room-pressure ( $NPT$ ) equilibration for 240 ps, during which the average box lengths are calculated. In a second relaxation step, the box size is changed to match the average calculated during the  $NPT$  relaxation, and each supercell is relaxed at a fixed temperature and constant volume ( $NVT$ ) for 10 ps. Finally, data is accumulated over 20 ps runs at constant volume and energy ( $NVE$ ). To reduce noise in the measured data by improving statistical sampling, three different simulations are run at each temperature, each one using the perfect crystal structure as a starting point, but with different initial atomic velocities.

The enthalpy  $H(T)$  is determined for each temperature  $T$  in K by taking its average over the  $NVE$  runs. For the purpose of comparison with experimental results, the reduced enthalpy increment

$$\Delta H^{\text{red}}(T) = \frac{H(T) - H(300)}{T - 300} \quad (1)$$

is deduced from these data points. The constant-pressure heat capacity  $C_P(T)$  is determined by differentiating the enthalpy

$$C_P(T) = \frac{\partial H}{\partial T} \quad (2)$$

This is carried out numerically using a first-order centred finite difference scheme. To limit numerical noise resulting from fluctuations of the measured enthalpy, a five-point Savitzky–Golay filter [47] was applied before taking the derivative. This results in no visible difference in the enthalpy curves, but improves the evaluation of the heat capacity. In a similar way, the linear thermal expansion coefficient

$$\alpha(T) = \frac{\partial \ln(a)}{\partial T} \quad (3)$$

is calculated using the measured lattice parameter  $a(T)$ , with the same protocol employed to calculate  $C_P(T)$ .

Equation (3) is used instead of the equivalent and more common expression  $\alpha = 1/a \partial a / \partial T$  for the increased numerical precision of its finite differences discrete form.

The atoms' trajectories calculated during the simulations are used to determine vibration spectra  $g(\varepsilon)$  by taking the Fourier transform of the velocity autocorrelation function (VAF). Partial spectra corresponding to the separate contributions from oxygen and uranium are calculated using partial VAFs.

Defects are detected and counted using an implicit Voronoi scheme, in which each atom is mapped to the closest lattice site in the perfect structure. If two atoms are mapped to the same site, then the atom further from the site is an interstitial. Conversely, each lattice site that is not associated with an atom is a vacancy. The number of defects for each temperature is obtained by averaging the number of defects in snapshots taken every ps during the 20 ps *NVE* simulations.

### 3. Lattice dynamics

LD calculations were carried out to characterize vibration modes and investigate their changes associated with the superionic transition. Instead of using the standard quasi-harmonic approximation to account for thermal expansion, the lattice parameter for each temperature was taken from the MD simulation results. Thus, the calculations partially but implicitly account for anharmonic effects. In particular, the dilation caused by the presence of oxygen defects is reproduced, which would be impossible using simple methods based on the quasi-harmonic approximation.

Because of their high computational cost, which results from the need to diagonalize the dynamical matrix of each structure, LD calculations have been restricted to the conventional unit cell for the perfect crystal. The  $k$ -points used to calculate the densities of states were generated using a  $60 \times 60 \times 60$  Monkhorst-Pack grid [48].

Each mode's contribution from both elements have been determined by projecting the polarisation vectors onto the relevant ionic degrees of freedom. Thus, partial spectra directly comparable to those obtained from MD can be calculated. In the same way, the relative contribution of both elements to each vibration mode can be quantified, offering additional information about the nature of any frozen mode.

The thermodynamic properties  $H$  and  $C_P$  were calculated using finite difference methods, as was the case for MD simulations. Phonon-related properties  $S_{\text{vib}}$  and  $C_V$  can also be calculated by integrating the vibration spectra.

## III. RESULTS

### A. Enthalpy and heat capacity

The enthalpy increment and constant-volume heat capacity show a well-behaved, low-temperature regime, up to 2000 K. This is well known experimentally, and over that range the enthalpy can be described using a polynomial function [2]. Another contribution to the enthalpy is also well documented, usually referred to as anomalous heat [35], the onset of which is reported around 2000 K [33]. This is consistent with MD simulations carried out using the CRG [42] and other potentials [12, 13]. Although this has been widely reported, it is presented here because it is one of the bases for our description of the superionic transition.

The enthalpy increment in Figure 1 shows a hump around 2500 K similar to the lattice parameter. In the lower-temperature range 300 K – 2000 K, the enthalpy is well reproduced by the polynomial

$$\begin{aligned} \tilde{H}_1(T) = & -13.5695 + 2.80400 \cdot 10^{-4} \cdot T \\ & - 2.22534 \cdot 10^{-8} \cdot T^2 + 1.59364 \cdot 10^{-11} \cdot T^3 \\ & - 2.392815 \cdot 10^{-15} \cdot T^4 + 1.32687 \cdot T^{-1} , \end{aligned} \quad (4)$$

which is a form similar to other fits available for  $\text{UO}_2$  [2]. The coefficients differ from previous calculations using the CRG potential [20], where a larger temperature range than that of equation (4) was considered to fit the enthalpy increment. This polynomial behavior changes at 2000 K, where the enthalpy starts increasing noticeably over that baseline. The excess enthalpy can be represented as an Arrhenius contribution, expressing the effect of the increase of the number of defects with temperature. Therefore, the enthalpy in the 2000 K – 2500 K range is well described by the form

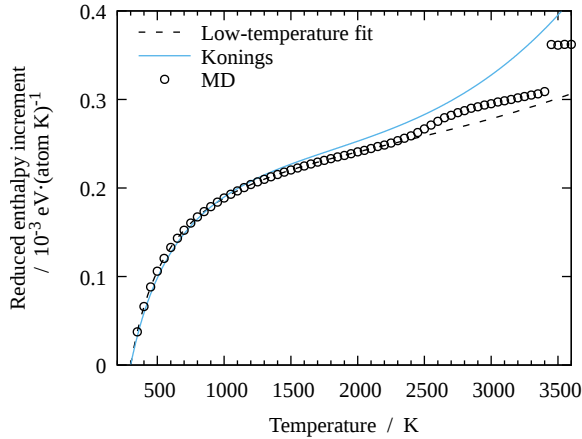
$$\tilde{H}_2(T) = \tilde{H}_1(T) + A \cdot e^{-\beta E_f/2} , \quad (5)$$

where  $E_f$  corresponds to the formation energy of the defects responsible for the anomalous heat and  $\beta = 1/k_B T$ . This additional contribution is of the same form proposed by Szwarc to model the effect of oxygen Frenkel pairs [35]. The fit for this exponential term shown in Figures 1 and 2 was obtained from defects populations, as will be described later. After a transition between 2500 K and 2800 K, the enthalpy follows another polynomial expression

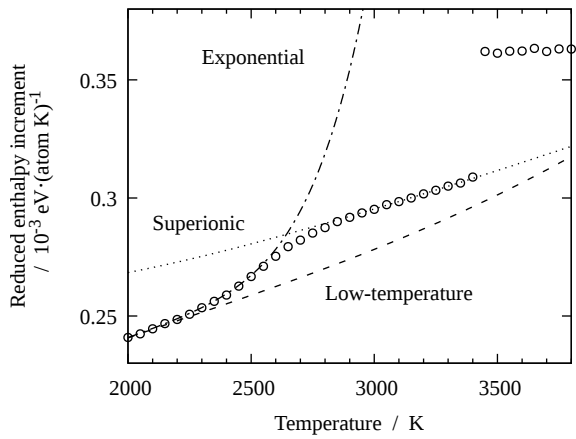
$$\begin{aligned} \tilde{H}_3(T) = & -13.2613 + 6.65045 \cdot 10^{-5} \cdot T \\ & 5.20425 \cdot 10^{-8} \cdot T^2 \end{aligned} \quad (6)$$

until a sharp step at 3425 K.

The heat capacity obtained by finite differences of the MD enthalpies, shown in Figure 2, agrees with the analytical derivatives of the enthalpy fits over their respective validity range. The numerical noise present in the enthalpy is magnified in the heat capacity. Because of



(a)



(b)

FIG. 1: Reduced enthalpy increment of  $\text{UO}_2$ : (a) whole temperature range (b) higher temperatures. The dots show results from MD simulations, the dashed line shows a fit to the low-temperature regime, the dotted line shows the sum of the low-temperature fit and the isolated defects contribution. The solid line is the reference fit [2].

this, the exact position of the  $\Lambda$  peak is difficult to locate accurately. However, it is still between 2500 K and 2600 K.

Thus, on the basis of enthalpy and heat capacity data, 4 temperature ranges can be distinguished:

1. below 2000 K: the material is in a perfect crystal state, with negligible defect populations and the enthalpy following  $\tilde{H}_1$  (equation 4);
2. 2000 K–2500 K: the material is still crystalline, but with a significant oxygen Frenkel pairs (OFP) concentration and its the enthalpy is  $\tilde{H}_2$  (equation 5);
3. 2500–3450 K:  $\text{UO}_2$  is in its superionic phase; the

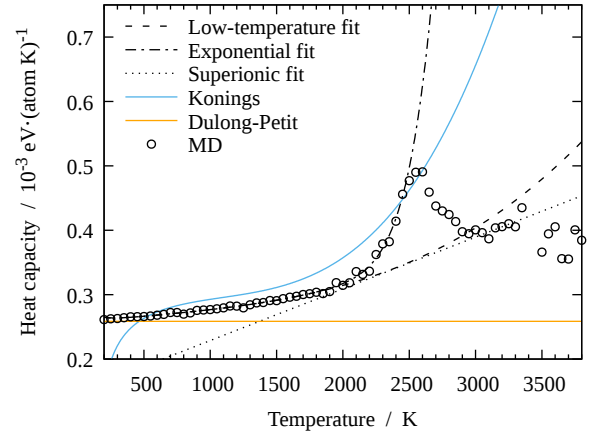


FIG. 2: Constant-pressure heat capacity of  $\text{UO}_2$  derived numerically from the enthalpy increment shown in figure 1. The solid blue line is the reference fit [2], and the solid orange line indicates the value expected from the Dulong–Petit law.

enthalpy converges to, and then follows,  $\tilde{H}_3$  (equation 6);

4. above 3450 K:  $\text{UO}_2$  is in its liquid phase, which is outside the scope of the present work.

## B. Thermal expansion

The temperature-dependent lattice parameter obtained from MD simulations is shown in figure 3a. A third-order polynomial

$$\tilde{a}(T) = 5.45259 + 5.5753 \cdot 10^{-5} \cdot T - 3.50256 \cdot 10^{-10} \cdot T^2 + 3.13032 \cdot 10^{-12} \cdot T^3 \quad (7)$$

was fitted to reproduce the lattice parameter in the lower-temperature range between 300 K and 2000 K, the same range identified for  $\tilde{H}_1$  in equation 4. This fit is in remarkable agreement with the recommendation from Martin [49], which is a fit based on several experimental studies. The expression for the linear thermal expansion coefficient in the low-temperature range can be derived from  $\tilde{a}(t)$ :

$$\tilde{\alpha}(T) = \frac{1}{\tilde{a}(T)} (5.5753 \cdot 10^{-5} - 7.00512 \cdot 10^{-10} \cdot T + 1.021875 \cdot 10^{-11} \cdot T^2) \quad (8)$$

This again shows good agreement with the reference fit [49].

As expected from previous studies using the same potential [50], a deviation from the lower-temperature behavior is observed from around 2000 K, with a hump on the lattice parameter curve in the 2000 K–3000 K

range. This is clearer in the linear thermal expansion coefficient shown in Figure 3c, where it appears as a sharp  $\Lambda$  peak with a maximum at  $2525 \pm 25$  K. This is another measure for the superionic transition temperature  $T_S$  predicted by the CRG potential.

It should be noted that the thermal expansion coefficient, and to a lesser extent the lattice parameter, exhibit noticeable noise above 2500 K. Nevertheless, the noise is in general lower than in the heat capacity and enthalpy data.

A sharp step is visible in the lattice parameter between 3450 K and 3475 K, which corresponds to melting. This is higher than the melting point measured using the moving interface method with the same potential,  $3050 \pm 50$  K [20], which is closer to the experimental values clustered around  $3030 \pm 20$  K [2]. It is well known that the type of simulation carried out here, starting from a perfect crystal, significantly overestimates melting points. This is because the limited length- and time-scales prevent nucleation of the liquid phase [51].

### C. Elastic constants

Significant structural changes tend to be associated with changes in the elastic constants. This is true, for example, for displacive phase transitions. The elastic constants are also linked to the stability of the structure via the Born criteria [52]: to be stable, a structure must exhibit  $C_{44} > 0$ ,  $(C_{11} - C_{12}) > 0$ , and  $(C_{11} + 2C_{12}) > 0$ . Because the superionic transition is characterized by extensive disorder on the oxygen sublattice, and therefore a form of instability, the elastic constants can provide some information about its behavior. The elastic constants relevant to the stability criteria,  $C_{44}$  and  $(C_{11} - C_{12})$ , calculated using LD with the lattice parameters measured from MD equilibration, are shown in Figure 4.

In the low-temperature regime, below 2000 K,  $C_{44}$  decreases slightly, in an almost linear fashion. Its behavior changes at 2000 K, where it starts to decrease more abruptly. Our calculations show an inflection point around 2500 K, followed by another quasi-linear decrease regime. Finally,  $C_{44}$  drops to zero at 3450 K, coincident with the appearance of the liquid phase. These features are broadly similar to those of the experimental data [40], which agree with our calculations on the magnitude of  $C_{44}$ . The main difference is that no inflection point is seen in the experimental curve. However, this could be explained by the limited accuracy of the measurements, particularly at high temperatures, and the proximity of the experimental melting point at 3100 K.

The evolution of the second stability indicator  $C_{11} - C_{12}$  is similar to that of  $C_{44}$ , both in the LD curves and the experimental data. However, there is some disagreement on the magnitude of  $C_{11} - C_{12}$  at low temperatures, which worsens as temperature increases and the experimental values decrease more rapidly than the sim-

ulations.

In any case, no discontinuity has been seen in the elastic constants, and the slope change at  $T_S$  in the LD calculations is minor and there is no drastic change in elastic properties. The limitation of these calculations is that although the expansion caused by the defects was taken into account, the contribution of the defects themselves was not.

### D. Static structure

The static structure was probed by calculating radial distribution functions (RDF) for the crystalline, superionic, and liquid phases, which are shown in Figure 5. As expected, the RDF at 2000 K shows a well-defined crystalline structure, with clear and sharp peaks with density gaps between them. In the liquid phase, here at 3500 K, both U-U and O-O RDFs have a first neighbor peak slightly shifted to larger distances compared to the crystal, due to the thermal expansion. The peaks in the liquid are also broad and short, but otherwise still visible. However, there are no clear minima after these peaks and the RDF tend to their long-range limit with small fluctuations.

The RDFs for the superionic phase, in the 2600 K–3400 K range, borrow features from both crystalline and liquid phases. The U-U curve still shows peaks at the neighbor distances, as in the crystal, but the minima between these peaks is greater than zero. The first peak is higher and better defined than that of the liquid. This indicates the presence of a lattice with significant local distortion and large thermal vibrations. The O-O curve, on the other hand, is very similar to that of the liquid phase. The first nearest neighbor peaks in both phases have the same height, and neither are followed by a visible minimum. Therefore, from a structural point of view, the superionic phase looks like a crystalline uranium lattice whose holes are filled with oxygen in a liquid or fluid state. This picture is very similar to the part-crystalline, part-liquid state described in some materials with specific bond hierarchies [32], and consistent with the liquid-state interpretation of the superionic transition [24, 53]. However, previous works showed that the oxygen sublattice retained some structure in the superionic phase, and even had coexisting local environments with different structures [18].

### E. Defects population

It has been shown that defects, and more specifically OFPs, play an important role in the deviation from the low-temperature described previously [11]. It is therefore necessary to consider defects populations to have a complete understanding of the changes in thermodynamical properties. The characteristics of point defects, such as formation energies, are generally well known in the low

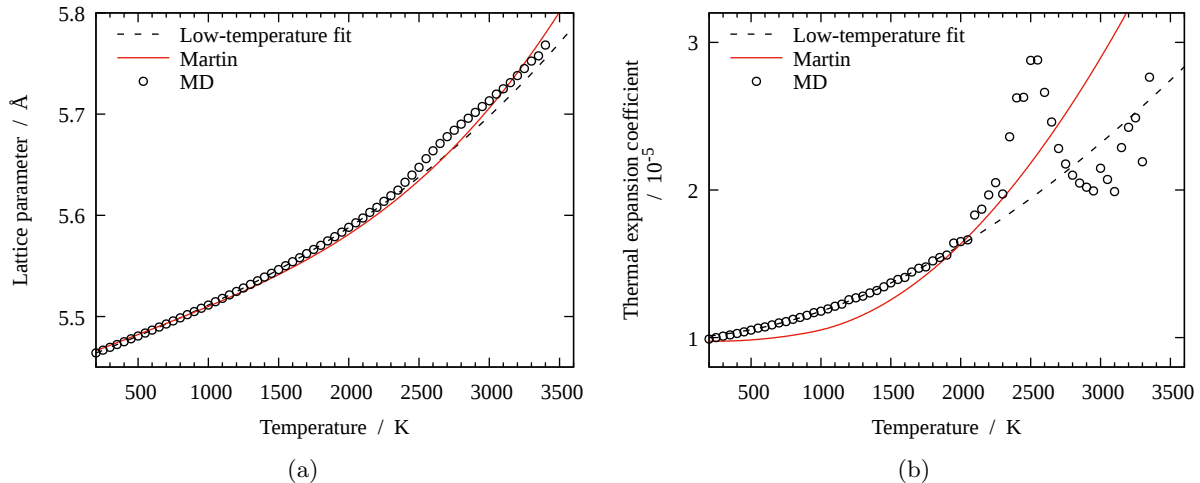


FIG. 3: Thermal expansion of  $\text{UO}_2$  as a function of temperature: (a) lattice parameter; (b) and linear thermal expansion coefficient. The points indicate values obtained from MD simulations, the dashed lines show fits to the low-temperature regime, and the solid lines show Martin's fit [49].

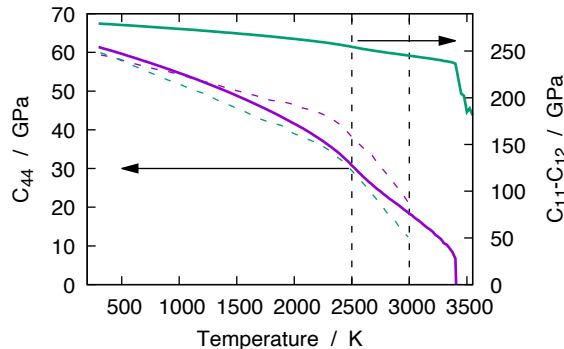


FIG. 4: Elastic constants in  $\text{UO}_2$ , calculated using lattice dynamics. Green curves show  $(C_{11} - C_{22})$  and purple curves show  $C_{44}$ . The dashed lines are from the reference [40].

temperature regime, with results from experiments [54], DFT simulations [55] as well as empirical potentials [56]. Uranium defects tend to be very unfavorable compared to oxygen defects, and OFPs are consistently the lowest energy defects, followed by Schottky defects [55, 57].

The defects observed in our simulations were mostly oxygen defects. Only a very small concentration of uranium defects were detected close to 3450 K. The fraction of OFPs measured in our simulation boxes are presented in Figure 6. No defects were detected in the low temperature regime below 2000 K. Whilst this is to some extent a result of the limited size of the simulation box — an equilibrium population of defects would be expected to be present in a macroscopic sample, but in a very small concentration. Defects can still be created by other means, *e.g.* radiation damage or non-stoichiometry. An exponential growth becomes noticeable above 2000 K, until

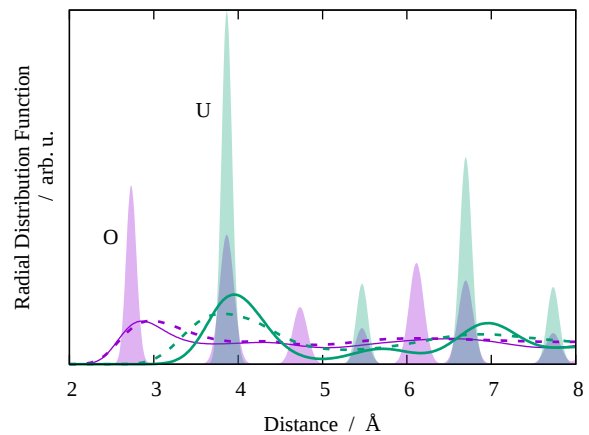


FIG. 5: Radial distribution functions for  $\text{UO}_2$  in different phases, calculated from MD simulations: shaded peaks show the RDF at 2000 K and indicate the crystal structure; dashed lines show the liquid at 3500 K; solid lines show the superionic structure at 3000 K. The purple curves are O–O distribution functions and the green curves are U–U.

about 2600 K. In this regime, the defect concentration followed the law  $\tilde{N}_f = N_0 \cdot e^{-\beta E_f}$ , where  $E_f$  is an effective formation energy for oxygen Frenkel pairs. By fitting to the MD number of defects, the value  $E_f = 7.3$  eV was found. This value was used in the fit of the enthalpy increment  $\tilde{H}_2(T)$  in Figure 1b and in the exponential regime of the heat capacity in Figure 2. Simulations have shown that the precise formation energy of an OFP is highly dependent on the defect's configuration, particularly the distance between the vacancy and the interstitial [55, 56, 58]. The simulation boxes used here are

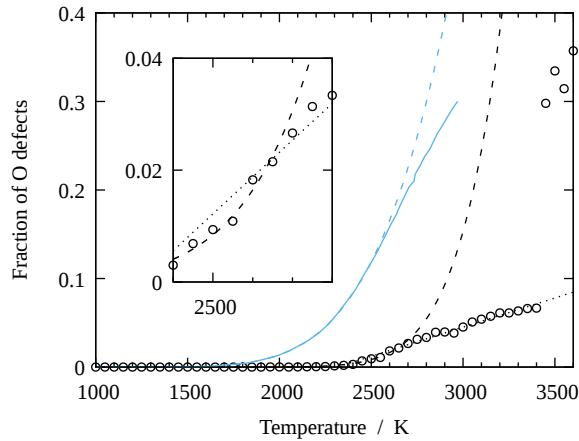


FIG. 6: Fraction of oxygen Frenkel pairs in  $\text{UO}_2$  from MD simulations. The dashed black line shows a fit to the defect concentrations in the Arrhenius regime; the dotted line shows a fit to the linear regime; the solid blue line shows defect numbers measured by Pavlov [11], and the dashed blue line is an Arrhenius fit in the relevant temperature range. The inset shows the crossover between exponential and linear regimes at 2600 K.

not large enough to consider the defects truly isolated, which could in principle cause the effective formation energy to deviate slightly from its value at the dilute limit. Moreover, the way defects are detected in our simulation can under-estimate their population, which makes this value difficult to compare directly to references, which are generally in the 3.5 eV–4.5 eV range. In particular, the best experimental data available show OFP energies of  $4.6 \pm 0.5$  eV [40] and 3.71 eV [11]. Even though the CRG potential is known to over-estimate the OFP energy, its value from static calculations is 5.73 eV [20], lower than the value of  $E_f$  we measured from MD data. For these reasons, the energy obtained from fitting to the defects population is an effective value, which does not correspond to a specific configuration and deviates from values obtained from static calculations usually reported. Nevertheless, deviation from exponential growth happens close to the superionic transition temperature  $T_S$ , which suggests that there is indeed a change in the mechanism for OFP creation at the superionic transition.

The exponential increase in defect concentrations stops around 2600 K, after which it follows a linear law until the appearance of the liquid phase. Thus, the defect concentration over the whole temperature range can be represented using the fit

$$\tilde{N}_f(T) = \begin{cases} A \cdot e^{-\beta E_f/2}, & T \leq 2600 \text{ K} \\ B \cdot T + C, & 2600 \text{ K} < T \leq 3425 \text{ K} \end{cases} \quad (9)$$

In the temperature range over which the concentration of OFPs increases exponentially, their contribution to the

enthalpy of the material can be estimated by considering that each defect contributes its formation energy. The resulting function is  $\Delta \tilde{H}_f = E_f N_0 e^{-\beta E_f/2}$ . The comparison with the enthalpy increment in Figure 1 and with the heat capacity in Figure 2 shows that this exponential factor is responsible for the exponential increase of the enthalpy increment between 2000 and 2500 K. However, defect population alone cannot explain the enthalpy at higher temperatures, which does not have a linear behavior.

An intuitive understanding of the end of the exponential regime is that the assumption about large separation between defects and the absence of interactions is no longer true. As the concentration of defects increase, they can either recombine and disappear, or arrange themselves into clusters. Therefore, a natural candidate to explain the transition and the linear regime is defects clustering or structure change. This is consistent with the understanding of the superionic transition as driven by the collapse of the anionic sub-structure following its saturation with point defects. Assuming a purely random distribution of oxygens on their cubic sub-lattices, under the constraint that no site can be occupied by more than two particles, the saturation OFP concentration is about 0.32. These assumptions are a simplification, but seem to be justified in light of our measurements and geometric considerations. And indeed, experimental OFP concentrations such as those from Pavlov *et al.* [11] reach half this saturation threshold at  $T_S$ , and come close to it near the melting point. In comparison, from calculations assuming that the superionic transition is caused by instability resulting from electrostatic interactions between defects we would expect a concentration of 0.26 at  $T_S$  [7]. However, this is clearly not the case in our simulations, where the fraction of defects is 0.02 at  $T_S$ , despite the superionic transition clearly happening. The current simulations are therefore consistent with oxygen defects saturation not being the mechanism behind the transition.

Some empirical laws have been proposed to correlate the OFP formation energy and the superionic transition, such as [7],

$$T_S \sim E_f/20 k_B. \quad (10)$$

This seems to work in  $\text{UO}_2$ , if one takes the experimental OFP formation energy of 4.5 eV, which would quite accurately predict  $T_S$  at 2610 K. However, this completely fails in the case of the CRG potential, which should have  $T_S = 4240$  K. It also does not work with Pavlov’s experimental OFP formation energy, which would correspond to  $T_S = 2150$  K, or with the Morelon potential [59], which has an accurate  $E_f = 4.45$  eV and yet has  $T_S$  around 2850 K [13] instead of 2480 K as equation (10) would predict. Thus, the correlation between OFP formation energy and the superionic transition temperature, based on the assumption of defect saturation, does not generally hold.

## F. Lattice vibrations

Vibration modes have been investigated using two different techniques: by calculating the phonon density of states from the velocity autocorrelation function accumulated over the duration of MD simulations on one hand (MD approach), and by calculating the eigenvalues and eigenvectors for a conventional cell (LD approach). To keep both approaches consistent, the unit cells for the LD calculations were scaled to reproduce the lattice parameter measured from room-pressure MD relaxations. Both types of calculations are complementary: MD spectra implicitly account for anharmonic effects such as phonon-phonon interactions, defects, and defect clusters, whilst LD offer much more information by making the whole polarisation vector available for each vibration mode. By using the MD lattice parameter, the polarisation vectors from LD calculations implicitly account for thermal expansion, which is a manifestation of anharmonicity. However, other anharmonic effects are missing.

Spectra obtained at 300 K using both approaches, shown in Figure 7a, agree very well with each other, as well as with spectra from other studies obtained from DFT-based LD calculations [60–63]. The dispersion curve in Figure 8a provides more detailed information. It shows the presence of three clearly distinct bands: band I with the acoustic modes in which both uranium and oxygen take part, band II with optical modes, with almost no contribution from the oxygen ions, and finally a high-energy band III composed of optical oxygen modes. This band structure is clearly visible on the dispersion curves at 300 K in Figure 8a, in which the color code indicates the relative contribution of oxygens. The low-temperature spectra show no visible overlap between bands II and III, although there is no band gap as sometimes reported in the literature [61]. This type of phonon band structure has been observed in compounds related from a structural point of view, such as  $\text{CeO}_2$  [30].

As temperature increases, a general softening of the modes in band III is observed, with the high-energy part of the oxygen spectrum being rigidly shifted towards lower energies. This is visible on both LD and MD spectra at 2 200 K shown in Figure 7b. Though, as expected, the agreement between LD and MD spectra worsens as temperature increases. Notably, the high-energy tail of band III is much longer, and the peaks are smaller and wider in the MD spectra. This longer tail at high energies is caused by high-frequency vibrations of the atoms neighboring interstitials and vacancies, and is therefore a consequence of the presence of defects, which are absent from the LD calculations. The peaks in bands I and II become sharper and taller as the temperature increases in LD calculations, whilst they shrink and spread in MD simulations. Band III seems to lose its structure, and no peak is visible by 2 200 K. The discrepancy is probably caused by phonon scattering by defects, which increases the line widths of individual modes. It cannot be explained by a structural change as it is already visible in

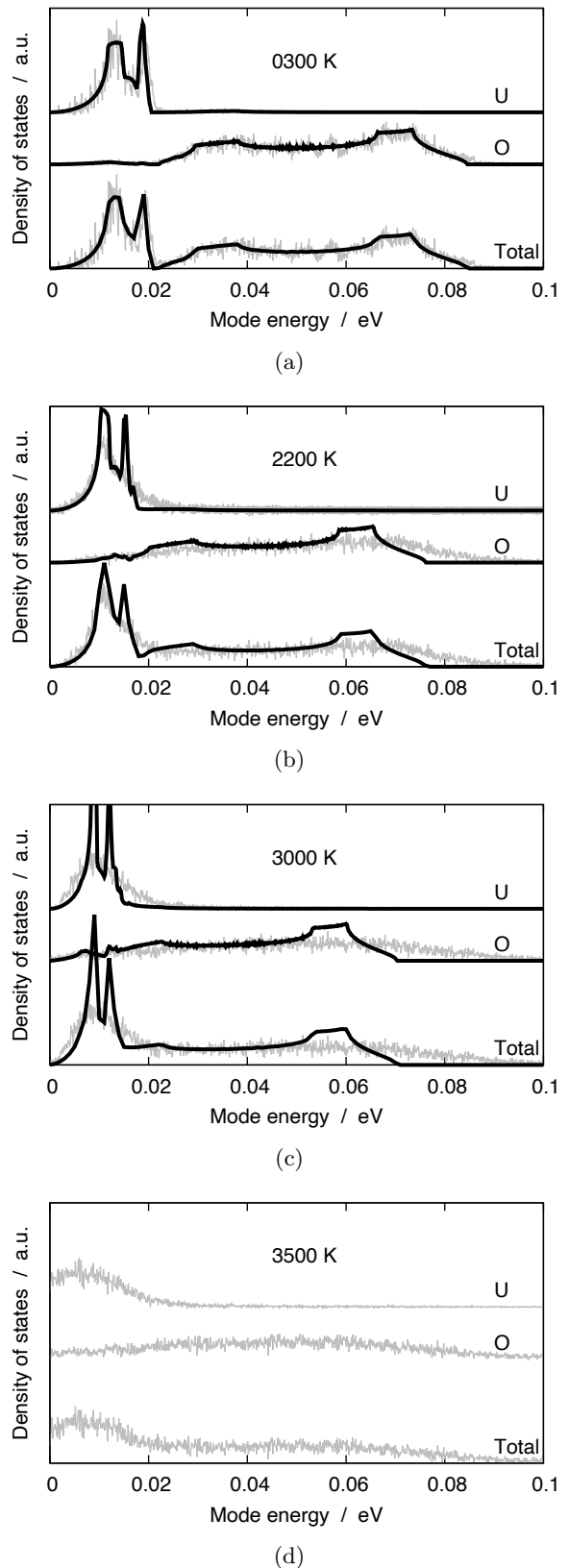


FIG. 7: Vibrational density of states in  $\text{UO}_2$  at different temperatures: (a) 300 K; (b) 2 200 K; (c) 3 000 K (superionic phase); (d) 3 500 K (liquid phase). Thin grey lines show densities of states calculated from MD simulations using velocity autocorrelations; thick black lines show densities of states from LD calculations.

the 2000 K – 2500 K range, where the only structural difference with the perfect crystal is isolated point defects.

The MD density of states does not show any qualitative change at the superionic transition, between 2200 and 3000 K. Moreover, even compared to the liquid phase at 3500 K on Figure 7d, the oxygen density of states is very similar to that of the superionic phase at 3000 K, as well as that of the high-temperature defective crystal at 2200 K.

### G. Modes softening

Some oxygen modes on the lower edge of band III undergo significantly more softening than the rest of the band, as can be seen when comparing Figures 8a and 8b. These modes become frozen, *i.e.* their frequency tends to zero, at  $2450 \pm 50$  K. Beyond that temperature, their frequencies as calculated in the LD framework becomes imaginary. At these temperatures, the  $8c$  tetrahedral sites of the  $Fm\bar{3}m$  structure, which are the oxygen sites in a perfect  $\text{UO}_2$  crystal, become mechanically unstable. This results in disorder in the oxygen sublattice as the force keeping the oxygens on their lattice sites vanish. The imaginary modes are low-energy optical (LEO) modes, with a wavevector corresponding to the X point of the Brillouin zone of the primitive unit cell, similarly as what was reported in  $\text{CeO}_2$  [30] and  $\text{Li}_2\text{O}$  [64]. The fact that the contribution to these modes from uranium ions is zero means that the instability resulting from these imaginary modes is confined to the oxygen sublattice. Thus, the uranium sublattice, and therefore the overall material, retains its structural integrity even as the oxygen sublattice breaks down.

The eigenvectors corresponding to these modes calculated with lattice dynamics, represented in Figure 8d, offer a complete description of the motion of the atoms involved. We can verify that this mode does not move any uranium ion. Moreover, it shows that the associated deformation is a specific distortion of the oxygen cube in the cell. All the particles involved move predominantly along a  $[100]$  axis in the conventional  $Fm\bar{3}m$  cubic cell. They also move in pairs, with both atoms on the same  $[100]$  edge moving towards the same direction, and adjacent, parallel edges moving in opposite directions.

The link between imaginary vibration modes and the onset of superionic transitions has been observed in materials with the fluorite structure such as  $\text{CeO}_2$  [30] or anti-fluorite structure such as  $\text{Li}_2\text{O}$  [64].

Increasing the lattice parameter further, to reproduce higher temperatures, there comes a point where the contribution from uranium to the imaginary modes becomes significant (see Figure 8c). This happens in an acoustic mode close to the  $\Gamma$  point along the  $[\zeta \zeta 0]$  line. At this point, both sublattices become unstable and collapse. This is the mechanical melting point  $T_M$  of the material [52]. The melting point measured experimentally and using the moving interface method with MD

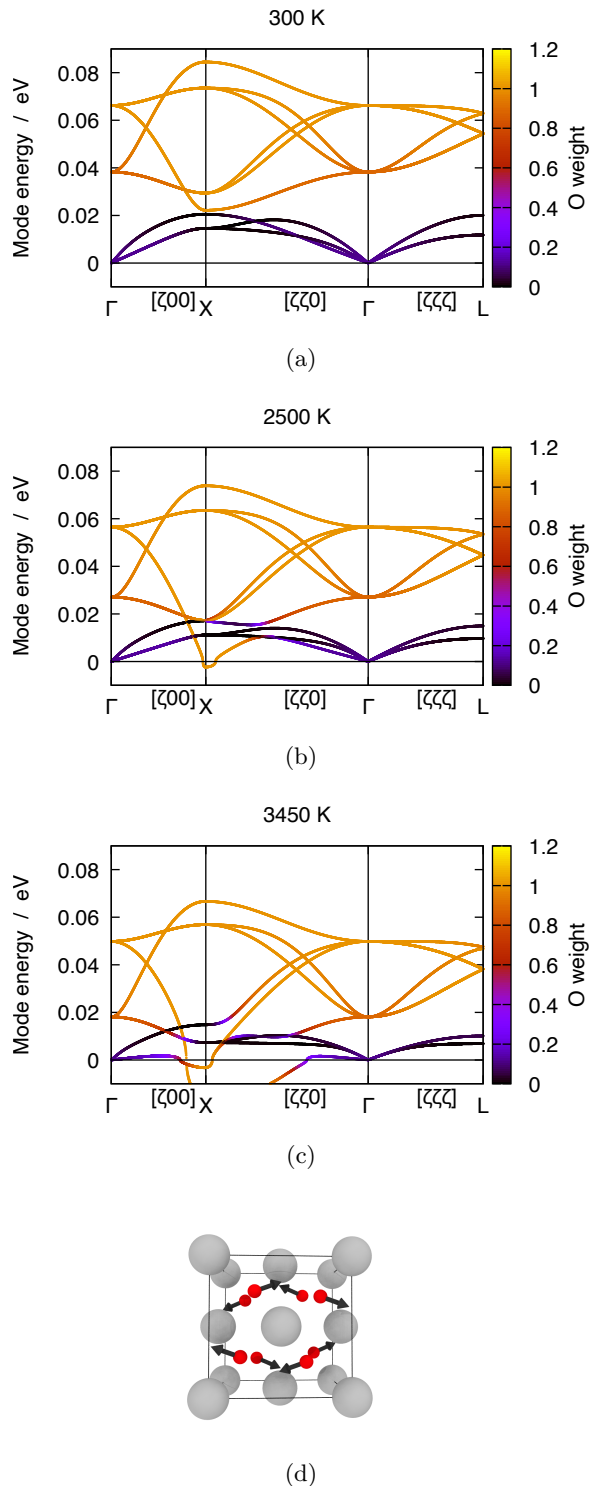


FIG. 8: Phonon dispersion curves in  $\text{UO}_2$  at different temperatures from LD simulations: (a) 300 K; (b) 2500 K, showing the imaginary LEO oxygen mode; (c) 3450 K, showing the mechanical melting of the material. Subfigure (d) shows a representation of the displacement associated with one of the LEO imaginary modes visible in the 2500 K dispersion curve. An animated version of this subfigure is available in the supplementary information.

simulations, and usually reported in the literature, is the thermodynamic melting point  $T_m$ . The difference between both melting points is that beyond  $T_m$ , the liquid phase is more stable from a thermodynamic point of view (*i.e.* it has a lower Gibbs free energy than the superionic and crystalline phases). But there is still an energy barrier to overcome to melt the material. This means that melting is thermally activated and usually happens at specific locations where a nucleation and growth process starts. For temperatures between  $T_M$  and  $T_m$ , the superionic phase is metastable. Given a nucleus, like in moving interface simulations, the liquid phase grows until it consumes the superionic phase. For temperatures greater than  $T_M$ , the superionic phase is unstable and small supercells or the lack of nucleus cannot prevent its melting, which is instantaneous over the whole simulation box.

### H. Lindemann parameter

The Lindemann parameter is a quantification of the disorder in thermal fluctuations of the atomic positions. It relies on the difference  $\mathbf{u}^\alpha$  between the position of each atom  $\alpha$  and its perfect crystal site. It can be defined for a subset  $A$  of the atoms in the structure of interest, as the root mean square of the norm of the displacement  $\mathbf{u}^\alpha$ , averaged over the atoms in  $A$

$$l_A = \frac{1}{d_{A-A}} \sqrt{\frac{1}{N_A} \sum_{\alpha \in A} \|\mathbf{u}^\alpha\|^2} \quad (11)$$

where  $d_{A-A}$  is distance between nearest neighbors in the  $A$  sublattice. The Lindemann criterion posits that a material reaches its melting point if this parameter reaches a critical value around 0.1 [65]. In practice, this value is somewhat material-dependent, but the criterion is useful to help investigate the onset of melting transitions. In the case of  $\text{UO}_2$ , both sublattices need to be treated separately, because they are loosely coupled and are dominated by different vibration modes, and thus are expected to be displaced by different magnitudes. The displacements  $\mathbf{u}^\alpha$  are calculated from the same Voronoi mapping used to quantify point defects. This is a simple, robust, and computationally inexpensive method. Its main limitation is that the reference lattice sites correspond to those of a perfect crystal. Thus, values for very highly-disordered or liquid phases cannot be interpreted quantitatively. This leaves, however, qualitative information that can be discussed to help understanding the changes that occur at the superionic transition.

The Lindemann parameters calculated in this way are shown in Figure 9. The uranium sublattice exhibits a simple and expected behavior, with  $l_U$  increasing monotonically until it jumps just below 3475 K, which is the mechanical melting temperature  $T_M$ . At this temperature,  $l_U$  is 0.12, which is the order of magnitude we would expect from the simple Lindemann melting criterion. This is not the case for the oxygen sublattice.

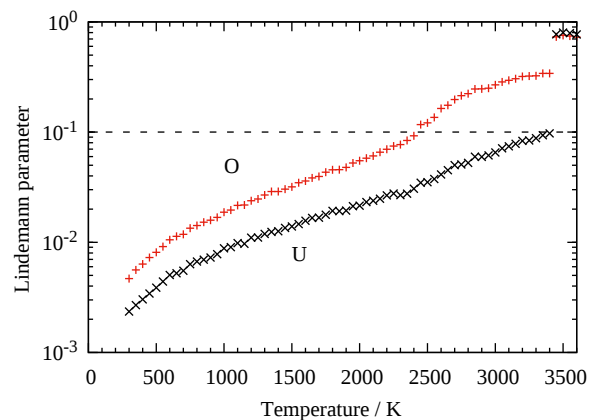


FIG. 9: Lindemann parameter for oxygens and uraniums in  $\text{UO}_2$ , over the temperature range considered in this study. The dashed line indicates the 0.1 value corresponding to the standard Lindemann melting criterion.

Overall,  $l_O$  is always greater than  $l_U$  calculated at the same temperature. Both datasets show similar behaviors for low temperatures. However, the oxygen sublattice shows signs of additional increase around 2000 K. This can be explained by the disorder induced by the point defects that start appearing at these temperatures and the associated lattice distortions. This increase tapers off between 2500 K and 2600 K, after which the parameter once again grows monotonically.

These observations underline the smooth transition from the low-temperature perfect crystal and the high-temperature superionic phase between 2000 K and 3000 K. Over this transition, the parameter jumps beyond the 0.1 value that could be considering as an indication of melting of the structure. There are, however, two main differences compared with a melting transition. The first is that this transition is smooth and the parameter varies continuously. This is in stark contrast with the true melting transition observed for the uranium sublattice at 3450 K, which does indeed show a step. The second observation is that even in the superionic temperature range, the oxygen Lindemann parameter is still far from its value in a true liquid, which it reaches at 3500 K, at the same time as  $l_U$ .

### I. Oxygen diffusion

Oxygen diffusion coefficients were calculated from mean squared displacements extracted from the MD simulations. The diffusion behavior in  $\text{UO}_2$  is very well known [12], including predictions using the CRG potential [50]. Diffusion in the perfect structure below 2000 K is low (smaller than  $10^{-9} \text{ cm}^2 \cdot \text{ps}^{-1}$  in our simulations), owing to the low concentration of oxygen

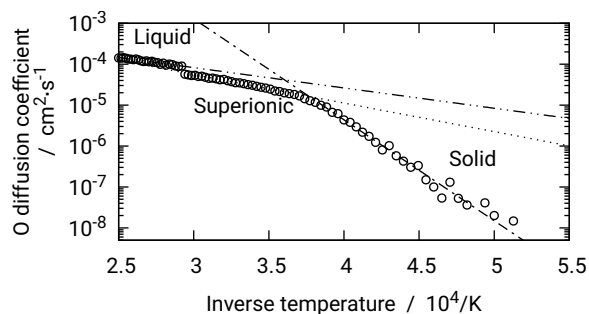


FIG. 10: Oxygen diffusion coefficient as a function of temperature in  $\text{UO}_2$ . The dotted lines show exponential fits corresponding to different temperature ranges.

defects. It increases in the 2000 K–2500 K range, with the exponential increase in concentration of OFPs. The activation enthalpy for diffusion in this range is 4.9 eV. This is an over-estimation compared to values from the literature, which are closer to 2.3 eV [12], but is consistent with other calculations using the CRG potential [42]. Beyond the superionic transition, another Arrhenius behavior is observed, but with a different pre-exponential factor and an activation enthalpy of 1.38 eV. The melting point is notable by the rate of change of the diffusion coefficient shown in Figure 10. However, whilst this is associated with a jump in the pre-exponential factor, the change in activation enthalpy is very small. Its value in the liquid phase is 0.98 eV, very close to the reference value of 0.95 eV [12]. The small difference between the activation enthalpies in the superionic and liquid phases is indicative that diffusion mechanisms in both phases are likely similar.

The van Hove correlation function [66] provides information on the diffusion mechanisms, beyond the average given by the diffusion coefficients. We calculated the self-contribution  $G_S(r, t)$ , which indicates the probability density that a particle has traveled a distance  $r$  over a time  $t$  during the simulation, and is shown in Figure 11 for  $t = 20$  ps and for different temperatures. Separate functions were calculated for oxygen and uranium ions,  $G_S^O$  and  $G_S^U$  respectively, to describe their different behaviors.

In a perfect crystal,  $G_S(r, t)$  shows a peak close to the origin on the distance axis, which goes to zero for distances shorter than the first neighbor distance  $r_{1\text{NN}}$ . This means that, although particles move because of thermal fluctuations, thus broadening the peak, the probability of one of them leaving its site is effectively zero:  $G_S(r > r_{1\text{NN}}, t) = 0$ . This is what we observed for  $\text{UO}_2$  in our simulation, and is shown for oxygens at 2000 K (Figure 11a), and for uraniums at 3000 K (Figure 11b). The opposite behavior is that of a liquid, in which case the small-distances peak disappears completely over very short time scales, leaving a broad hump that widens and

shifts to larger distances as time increases. This was observed as expected above the mechanical melting point, for example for uranium ions at 3500 K (Figure 11b).

The superionic phase shows a combination of both archetypical behaviors. On the uranium sublattice, no significant diffusion occurs before the melting point, and only a small number of cations are displaced, resulting in a very small amount of numerical noise in  $G_S^U(r, t)$  around 3400 K. The melting transition is unmistakable and occurs between 3400 and 3500 K, with very small changes before that. On the anion sublattice, however, the picture is drastically different. The characteristics of a perfect crystal with very low diffusion is retained until about 2200 K. Then, a secondary peak becomes noticeable at 2300 K, at a distance of  $\sim 2.9$  Å, which is  $a/2$ , or the first neighbor distance on the cubic anion sublattice. The minimum between these two peaks, indicating the spatial extent of the oxygen sites and the inner radius of the first neighbor shell, is close to  $a/3$ . The initial peak decreases significantly in magnitude as the secondary peak raises with increasing temperature. A very small tertiary peak is visible at 4 Å and 2500 K, which corresponds to the second nearest neighbor distance. However, these three peaks disappear as temperature increases, leaving only the broad signature of a liquid phase at 3000 K. This indicates that, although the behavior of the oxygen ions seem very similar to that of a liquid at 3000 K (and beyond, to the liquid phase), crystal-like diffusion mechanisms remain visible at 2500 K, which is the peak of the superionic transition. Thus, up until around the superionic transition temperature, diffusion can be explained by a hopping mechanism between adjacent oxygen sites at the time-scale of 20 ps. The uranium sublattice, which remains largely intact right until the melting point, is expected to constrain the oxygen diffusion by preventing anions from coming too close to the cation sites, which could be a cause for crystal-like features in the van Hove correlation functions. However, despite this,  $G_S^O(r, 20\text{ ps})$  is indistinguishable from that of a liquid at 3000 K.

## J. Dynamical structure

The van Hove functions discussed previously provide details on the diffusion of both uranium and oxygen ions. However, it is difficult to extract from them information about kinetics and how the structure changes over time. To do this, we defined two population of oxygen ions: static and mobile oxygens, or SO and MO respectively. The former are oxygens that did not move beyond their initial lattice site, whereas the latter have moved into the first neighbor shell of their initial site. To estimate both populations, we use a distance criterion, with mobile atoms having a displacement greater than  $a(T)/3$ . This is somewhat arbitrary, as the initial peak first neighbor peaks overlap, as can be seen in Figure 11a. However, slight changes in the displacement radius do not change the trend of the results. Their respective populations

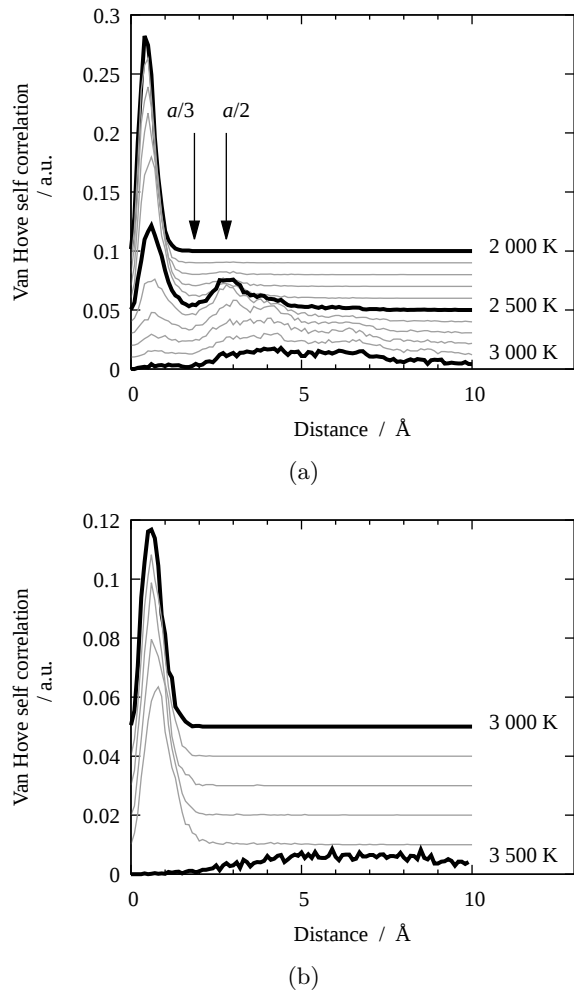


FIG. 11: Van Hove self-correlation functions in  $\text{UO}_2$  after 20 ps of simulation time showing the effect of temperature: (a) oxygen during the superionic transition; (b) uranium below and at the melting point. The curves have been shifted vertically to help with visual comparison. Successive lines correspond to temperature increments of 100 K.

change with time, as none of the ions are mobile initially. The uranium ions, with a very low mobility below the melting point are not considered in this analysis.

For each time-scale considered, the MO fraction as a function of temperature, shown in Figure 12b, presents a sigmoid shape, starting from zero at 2000 K, and tending asymptotically towards 1, close to the melting point. The inflection point is close to  $T_S$ , separating the two regimes. Below  $T_S$ , the MO fraction can be represented by an exponential function proportional to  $e^{-\beta E_f t/2}$ , where  $E_f$  is the formation energy for oxygen Frenkel pairs calculated previously. This is consistent with the premise that in the 2000 K – 2500 K range, mobility is driven by mechanisms involving individual Frenkel pairs. This linear relationship between mobility and number of defects

breaks down at  $T_S$ .

At a given temperature, the fraction of MO is expected to increase with time, until it reaches a threshold asymptotically. In the case of  $\text{UO}_2$ , as shown in Figure 12a, this threshold would be 1 if all the anions are mobile over the long term, or smaller if some of the oxygens remain immobile. The rate at which the MO fraction approaches the threshold increases with temperature and the associated mobility increases. A characteristic time  $\tau(T)$  can be defined as the time at which half the the oxygen ions have been displaced, *i. e.*

$$\frac{[\text{MO}]}{[\text{O}]} = \int_0^{a/3} G_S^{\text{O}}(r, \tau) dr = \int_{a/3}^{\infty} G_S^{\text{O}}(r, \tau) dr = \frac{1}{2} \quad (12)$$

This is a quantification of the time-scale over which the oxygen substructure retains the memory of its initial state. After this time, more than half the oxygen ions have swapped positions and are now occupying lattice sites different from their initial ones, even though the overall structure of the material remains similar. This characteristic time decreases with increasing temperature, following the expression

$$\tau(T) = a/(T - T_0) \quad (13)$$

until the crystal melts at  $T_M$ , at which point it has a small step. We could not measure  $\tau$  below 2500 K, because of the time scale of our simulations. Fitting equation (13), we obtain a critical temperature  $T_0 = 2550$  K, at which  $\tau$  tends to infinity.

The fraction of MO at a given time can also be considered as a function of temperature, as in Figure 12b. As would be expected, it increases with temperature, as overall oxygen mobility increases. In the lower end of the temperature range, between 2000 and 2500 K, the MO concentration increases exponentially, proportional to the OFP concentration in  $e^{\beta E_f t/2}$  discussed previously. This is consistent with a dominant diffusion mechanism involving individual point defects. At a given time each defect can swap position with one of its neighbors, thereby resulting in a number of displaced ions proportional to the number of defects. There is an inflection point at the superionic transition, between 2500 and 2600 K. In the superionic phase, the rate of growth of MO concentration decreases as it approaches 1. This is another indication of the change of diffusion mechanism at the superionic transition, consistent with the well-documented change in the activation energy for diffusion at  $T_S$  [12].

The spatial distribution of MOs can be investigated by counting the number of times the occupying ion is replaced on each lattice site. Thus, we can see “hot” sites (which occupying ion changes frequently) and “cold” sites (which are occupied by the same ion for longer periods of time). This is similar to techniques that are commonly used in studies on glass-forming and supercooled liquids [67]. This analysis provides a visual representation of the heterogeneity of diffusion in the material, as

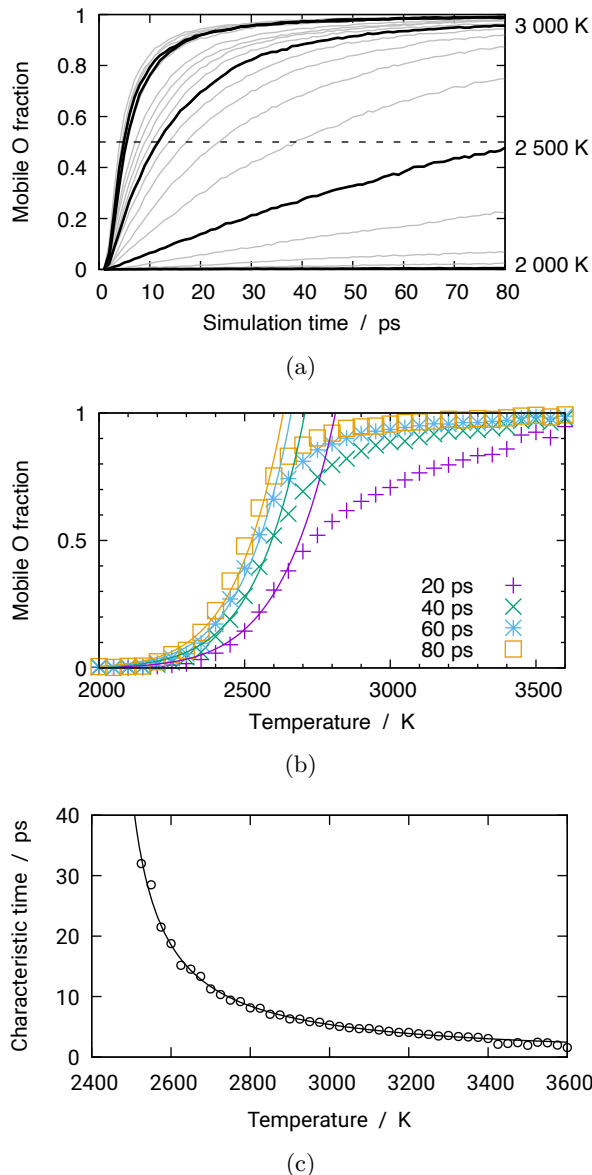


FIG. 12: Dynamics of oxygen ions in  $\text{UO}_2$  at high temperatures: (a) fraction of mobile oxygens as a function of simulation time, for temperatures every 100 K; (b) fraction of mobile oxygens as a function of temperature for different observation time-scales; (c) characteristic relaxation time for the oxygen sublattice.

shown in Figure 13. In this picture, a slice from a supercell taken during a simulation at 3000 K is divided into cubes centred on the oxygen sites of the perfect  $Fm\bar{3}m$  structure. The gray scale shows the number of different atoms having occupied each site over the course of 5 ps. This time-scale has been chosen because it corresponds to the value of  $\tau$  for that temperature. The distribution of hot and cold sites is clearly heterogeneous, forming clusters or pockets. Superimposed on these sites are the 5% most mobile atoms, showing their distribution rela-

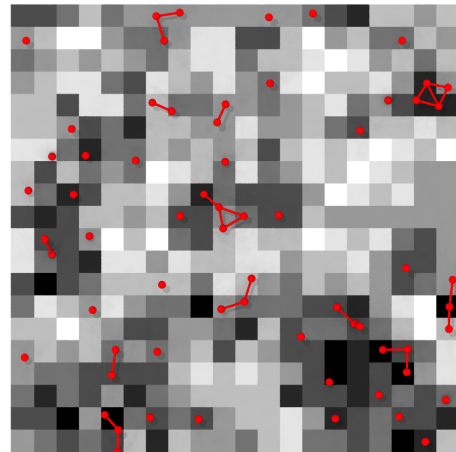


FIG. 13: Slice of a simulation box at 3000 K showing the displacement of oxygen ions over 5 ps. The color of each square indicates how many times its occupying oxygen has changed. The balls and sticks show the 5% most mobile oxygens in the slice and their clusters.

tive to the hot channels. The heterogeneous character of the distribution of mobile anions in superionic  $\text{UO}_2$  has been discussed in other studies, in which the presence of “strings” of highly mobile ions was observed [15, 16]. However, this picture only accounts for the 5% most mobile oxygens. Our simulations show that the dynamical behavior of the oxygens in superionic  $\text{UO}_2$  is close to that of a correlated supercooled fluid over time scales of the order of 5 to 10 ps.

#### IV. DISCUSSION

Using a combination of MD simulations and LD calculations, we can explain several aspects of the superionic transition in  $\text{UO}_2$ , as well as some characteristics of the superionic phase.

The properties of  $\text{UO}_2$  in the 2000 K – 2500 K temperature range can be explained by the population of oxygen Frenkel pairs we would expect considering their energy of formation in the 3.0 eV – 4.6 eV range [57]. Indeed, these temperatures are characterized by an exponential growth of OFP population, with a consistent exponential growth of the enthalpy and heat capacity. These defects also increase the thermal expansion of the lattice, and are an important cause of the observed anharmonic effects [35]. The behavior in this temperature range is well-known experimentally, and our results are completely consistent with the available references, with the caveat that the high formation energy of OFPs using the CRG potentials results in under-estimated defects populations compared to experiments. In addition, the OFP-induced thermal expansion causes significant softening of the LEO oxygen

normal modes, which are critical to explain the superionic transition in  $\text{UO}_2$ .

The superionic transition temperature  $T_S$ , at least in  $\text{UO}_2$ , coincides with these soft modes becoming imaginary, resulting in a fundamental instability of the oxygen sublattice. The transition itself appears as a second-order phase transition, with an inflection point in both enthalpy and lattice parameter at 2600 K, associated with a singular point in the heat capacity and thermal expansion coefficient. This resembles displacive phase transitions, also resulting from unstable vibration modes, such as those already documented for  $\text{UO}_2$  [68]. In particular, the transition to a  $Pbcn$  structure presents striking similarities with the superionic transition: both of them happen at similar deformations from the ground structure at 300 K, and both of them involve similar collective motion of oxygens, resulting in a disruption of the  $Fm\bar{3}m$  oxygen sublattice. However, whereas the  $Pbcn$  transition is between two crystalline structures, the superionic transition leads to a state with a combination of different local environments and that shares some dynamical features with glass-forming liquids. In this sense it is more similar to a mechanical melting [52, 69], when a crystal collapses because of its mechanical instability [70, 71], except that it involves only one sublattice and not the whole crystal. Contrary to thermodynamical melting, which requires nuclei of the liquid phase and is favored by defects or interfaces [72], the superionic transition occurs over the whole sample and does not require a nucleation and growth regime of the superionic phase. This is the reason why schemes such as the moving interface method have to be devised to make melting point measurements accurate and reproducible [43]. Furthermore, this also casts doubts on the interpretation of the superionic transition as resulting from the accumulation of oxygen defects leading to a collapse of the anion sublattice. Indeed, our simulations show that the transition does not correlate with a saturation at  $T_S$ , and the defect population kept growing with temperature in the superionic phase. Moreover,  $T_S$  from our simulation is very close to experimental values, despite the CRG potential significantly over-estimating the formation energy for OFPs, resulting in a much smaller defects population than in experiments, even at  $T_S$ . This indicates that, whilst defects contribute indirectly to the transition by enhancing thermal expansion, they are not a direct cause, and the structure itself, without any defect, is unstable at the volume  $\text{UO}_2$  reaches at 2600 K. In addition, at that temperature the Lindemann parameter for the oxygen sublattice is close to 0.1, which is the traditional criterion for melting. Thus, the superionic transition presents several aspects associated with melting, and yet remains a second-order transition with the uranium sublattice responsible for the structural integrity of the material, which prevents the discontinuity in both enthalpy and lattice parameters associated with true melting. At the upper end of the temperature range considered here, we observed mechanical melting of the uranium sublattice

at 3475 K, which is about 400 K above the thermodynamical melting point  $T_m$  predicted for  $\text{UO}_2$  by the CRG potential [20].

In the same way as the transition itself has seemingly contradictory characteristics, the characterisation of the superionic phase is challenging. In several respects, the properties of the superionic phase follow those of the lower-temperature crystalline phase. For example, the thermal expansion coefficients have similar behavior and are almost in continuity of each other. The structure itself is not distorted at the macroscopic level, and is still cubic with a FCC cation sublattice, with a  $Fm\bar{3}m$  structure. The oxygen ions are still more likely to be found close to  $Fm\bar{3}m$  8c tetrahedral sites. The elastic properties do not seem to suffer from a large drop caused by the instability of the oxygen sublattice. On the other hand, the oxygen sublattice looks very much like a liquid by certain aspects, like its pair distributions and van Hove correlation functions. Moreover, the dynamic behavior of this sublattice depends on the time scale at which it is considered. At short times, it behaves like a solid overall, in which ions tend to stay on their lattice sites. Then, after a temperature-dependent characteristic time, the memory of the initial positions is lost, which is illustrated by a van Hove function being close to that of a liquid. The distribution of active diffusion sites also presents some similarities with glass-forming liquids, with hot channels in which ions are replaced frequently, surrounded by pockets in which atoms are much less mobile. Such systems are known for their complex relaxation modes, which involve clusters of up to a dozen atoms, and different characteristic times.

Overall, this phase is analogous to part-crystalline/part-liquid materials such as some perovskites [73], other fluorites [53], and other materials with marked chemical bond hierarchies [32]. This understanding of the superionic phase is consistent with the observation of heterogenous mobility and diffusion mechanisms involving string-like ions clusters [15, 16].

## V. CONCLUSION

Our study reveals several intricate aspects of the superionic transition in  $\text{UO}_2$ . The transition is not driven by defect accumulation but rather by an inherent instability at elevated temperatures. Despite being categorized as a second-order transition, it exhibits characteristics reminiscent of melting, such as a high Lindemann parameter for the oxygen sublattice. However, the uranium sublattice maintains structural integrity, preventing discontinuities in enthalpy and lattice parameters typically associated with true melting. Above 3475 K, the uranium sublattice loses stability and mechanical melting is observed.

The superionic phase presents a blend of crystalline and liquid properties. It retains the overall cubic struc-

ture ( $Fm\bar{3}m$ ) and elastic properties similar to those at lower temperatures but exhibits liquid-like behavior in its oxygen sublattice dynamics, as evidenced by pair distributions and van Hove correlation functions. The dynamic behavior of this sublattice is time-scale dependent, behaving like a solid on short timescales and exhibiting fluid-like behavior over longer periods. The observed mobility patterns resemble those in glass-forming liquids, with highly mobile ions forming channels and pockets.

Overall, the superionic phase in  $\text{UO}_2$  is analogous to part-crystalline/part-liquid materials found in some perovskites, fluorites, and other systems with strong bond hierarchies. This understanding aligns with observations of heterogeneous mobility and diffusion mechanisms involving string-like ion clusters. However, it may seem at odds with the observation of hexagonal structural pat-

terns in the superionic phases of compounds with the fluorite structure [18]. These findings highlight the complexity and unique characteristics of this phase transition, offering insights into the behavior of  $\text{UO}_2$  at high temperatures.

## ACKNOWLEDGMENTS

PCMF would like to thank Dr Alain Chartier for his very helpful ideas and suggestions. The calculations presented here were run on the Blake cluster at CEA-Saclay. The unit cell in Figure 8d, as well as the pictures used to generate the videos in the electronic supplementary information were made with Ovito [74].

- 
- [1] J. K. Fink, *J. Nucl. Mater.* **279**, 1–18 (2000).
- [2] R. J. M. Konings, O. Beneš, A. Kovács, D. Manara, D. Sedmidubský, L. Gorokhov, V. S. Iorish, V. Yungman, E. Shenyavskaya, and E. Osina, *J. Phys.Chem. Ref. Data* **43**, 013101 (2014).
- [3] C. Guéneau, A. Chartier, L. Van Brutzel, P. C. M. Fossati, and P. Martin, in *Comprehensive Nuclear Materials* (Elsevier, 2020).
- [4] A. Dworkin and M. A. Bredig, *J. Phys. Chem.* **72**, 1277–1281 (1968).
- [5] M. A. Bredig, *Colloq. Int. CNRS* **205**, 183–191 (1972).
- [6] C. Ronchi and G. J. Hyland, *J. Alloy Comp.* **213**, 159–168 (1994).
- [7] N. H. March, D. D. Richardson, and M. P. Tosi, *Solid State Commun.* **35**, 903–905 (1980).
- [8] L. Leibowitz, L. Mishler, and M. Chasanov, *J. Nucl. Mater.* **29**, 356–358 (1969).
- [9] J. Ralph, *J. Chem. Phys.* **83**, 1253–1262 (1987).
- [10] J. P. Hiernaut, G. J. Hyland, and C. Ronchi, *Int. J. Thermophys.* **14**, 259–283 (1993).
- [11] T. R. Pavlov, M. R. Wenman, L. Vlahovic, D. Robba, R. J. M. Konings, P. Van Uffelen, and R. W. Grimes, *Acta Mater.* **139**, 138–154 (2017).
- [12] E. Yakub, C. Ronchi, and D. Staicu, *J. Chem. Phys.* **127**, 094508 (2007).
- [13] S. I. Potashnikov, A. S. Boyarchenkov, K. A. Nekrasov, and A. Y. Kupryazhkin, *J. Nucl. Mater.* **419**, 217–225 (2011).
- [14] S. Starikov and M. Korneva, *J. Nucl. Mater.* **510**, 373–381 (2018).
- [15] A. Annamareddy and J. Eapen, *Sci. Rep.* **7**, 44149 (2017).
- [16] A. Annamareddy and J. Eapen, *J. Nucl. Mater.* **483**, 132–141 (2017).
- [17] H. Zhang, X. Wang, and J. Douglas, *J. Chem. Phys.* **151**, 071101 (2019).
- [18] P. C. M. Fossati, A. Chartier, and A. Boulle, *Frontiers Chem.* **9**, 723507 (2021).
- [19] C. O. T. Galvin, M. W. D. Cooper, M. J. D. Rushton, and R. W. Grimes, *Sci. Rep.* **6**, 36024 (2016).
- [20] M. W. D. Cooper, M. J. D. Rushton, and R. W. Grimes, *J. Phys.: Cond. Matter* **26**, 105401 (2014).
- [21] D. Bathellier, M. Lainet, M. Freyss, P. Olsson, and E. Bourasseau, *Phys. Stat. Solidi B* **549**, 152877 (2021).
- [22] P. S. Ghosh, N. Kuganathan, C. O. T. Galvin, A. Arya, G. K. Dey, B. K. Dutta, and R. W. Grimes, *J. Nucl. Mater.* **479**, 112–122 (2016).
- [23] D. G. Frost, C. O. Galvin, M. W. D. Cooper, E. G. Obbard, and P. A. Burr, *J. Nucl. Mater.* **528**, 151876 (2020).
- [24] C. Takoukam-Takoundjou, E. Bourasseau, and V. Lachet, *J. Nucl. Mater.* **534**, 152125 (2020).
- [25] C. Takoukam-Takoundjou, E. Bourasseau, M. J. D. Rushton, and V. Lachet, *J. Phys.: Condens. Matter* **32**, 505702 (2020).
- [26] D. Bathellier, *Calcul des propriétés thermodynamiques et des défauts ponctuels dans les combustibles oxydes mixtes : approche couplée méthodes de structure électronique et potentiels interatomiques empiriques*, Ph.D. thesis, Université Aix-Marseille (2021).
- [27] G. Porto, J. Bouchet, D. Bathellier, J. Bodin, M. Canducci, J. Tranchida, P. C. M. Fossati, P. Martin, and E. Bourasseau, *J. Nucl. Mater.* **598**, 155163 (2024).
- [28] B. F. Naylor, *J. Amer. Chem. Soc.* **67**, 150–152 (1945).
- [29] P. Goel, N. Choudhury, and S. L. Chaplot, *Phys. Rev. B* **70**, 174307 (2004).
- [30] J. Klarbring, N. V. Skorodumova, and S. I. Simak, *Phys. Rev. B* **97**, 104309 (2018).
- [31] K. Wakamura, *Phys. Rev. B* **56**, 11593 (1997).
- [32] W. Qiu, L. Xi, P. Wei, X. Ke, J. Yang, and W. Zhang, *Proc. Mat. Acad. Sci.* **111**, 15031–15035 (2014).
- [33] D. A. MacInnes and C. R. A. Catlow, *J. Nucl. Mater.* **89**, 354–358 (1980).
- [34] P. Ruello, L. Desgranges, G. Baldinozzi, G. Calvarin, T. Hansen, G. Petot-Ervas, and C. Petot, *J. Phys. Chem. Solids* **66**, 823–831 (2005).
- [35] R. Szwarc, *J. Phys. Chem. Solids* **30**, 705–711 (1969).
- [36] R. J. Thorn, G. Winslow, and J. Ziomek, *J. Nucl. Mater.* **87**, 416–418 (1979).
- [37] J. Harding, P. Masri, and A. Stoneham, *J. Nucl. Mater.* **92**, 73–78 (1980).
- [38] P. Browning, G. J. Hyland, and J. Ralph, *High Temp.—High Press.* **15**, 168–178 (1983).
- [39] K. Clausen, W. Hayes, J. E. Macdonald, R. Osborn, and M. T. Hutchings, *Phys. Rev. Letters* **52**, 1238–1241

- (1984).
- [40] M. T. Hutchings, *J. Chem. Soc., Faraday Trans. 2* **83**, 1083–1103 (1987).
- [41] M. W. D. Cooper and M. J. D. Rushton, Potential model for actinide oxides and their solid solutions, <http://abulafia.mt.ic.ac.uk/potentials/actinides/v1.2> (2014).
- [42] M. W. D. Cooper, S. T. Murphy, P. C. M. Fossati, M. J. D. Rushton, and R. W. Grimes, *Proc. R. Soc. A* **470**, 20140427 (2014).
- [43] C. O. T. Galvin, P. A. Burr, M. W. Cooper, P. C. Fossati, and R. W. Grimes, *J. Nucl. Mater.* **534**, 152127 (2020).
- [44] D. Wolf, P. Keblinski, S. R. Phillpot, and J. Eggebrecht, *J. Chem. Phys.* **110**, 8254–8282 (1999).
- [45] S. J. Plimpton, *J. Comp. Phys.* **117**, 1–19 (1995).
- [46] M. E. Tuckerman, J. Alejandre, R. López-Rendón, A. L. Jochim, and G. J. Martyna, *J. Phys. A* **39**, 5629–5651 (2006).
- [47] A. Savitzky and M. J. E. Golay, *Anal. Chem.* **36**, 1627–1639 (1964).
- [48] H. J. Monkhorst and J. D. Pack, *Phys. Rev. B* **13**, 5188–5192 (1976).
- [49] D. G. Martin, *J. Nucl. Mater.* **152**, 94–101 (1988).
- [50] M. W. D. Cooper, S. T. Murphy, M. J. D. Rushton, and R. W. Grimes, *J. Nucl. Mater.* **461**, 206–214 (2015).
- [51] K. Govers, S. Lemehov, M. Hou, and M. Verwerft, *J. Nucl. Mater.* **376**, 66–77 (2008).
- [52] J. Wang, J. Li, S. Yip, and D. Wolf, *Phys. A* **240**, 396–403 (1997).
- [53] M. Makur and S. Ghosh, *Pramana J. Phys.* **35**, 151–157 (1990).
- [54] H. Matzke, *J. Chem. Soc., Faraday Trans. 2* **83**, 1121–1142 (1987).
- [55] M. Freyss, T. Petit, and J.-P. Crocombette, *J. Nucl. Mater.* **347**, 44–51 (2005).
- [56] K. Govers, S. Lemehov, M. Hou, and M. Verwerft, *J. Nucl. Mater.* **366**, 161–177 (2007).
- [57] J.-P. Crocombette, *Phys. Rev. B* **85** (2012).
- [58] L. Van Brutzel, A. Chartier, and J. P. Crocombette, *Phys. Rev. B* **78** (2008).
- [59] N.-D. Morelon, D. Ghaleb, J.-M. Delaye, and L. Van Brutzel, *Phil. Mag.* **83**, 1533–1555 (2003).
- [60] M. Sanati, R. C. Albers, T. Lookman, and A. Saxena, *Phys. Rev. B* **84** (2011).
- [61] Y. Yun, D. Legut, and P. M. Oppeneer, *J. Nucl. Mater.* **426**, 109–114 (2012).
- [62] B.-T. Wang, P. Zhang, R. Lizárraga, I. Di Marco, and O. Eriksson, *Phys. Rev. B* **88** (2013).
- [63] J. W. L. Pang, A. Chernatynskiy, B. C. Larson, W. J. L. Buyers, D. L. Abernathy, K. J. McClellan, and S. R. Phillpot, *Phys. Rev. B* **89** (2014).
- [64] M. K. Gupta, P. Goel, R. Mittal, N. Choudhury, and S. L. Chaplot, *Phys. Rev. B* **85** (2012).
- [65] F. A. Lindemann, *Phys. Z.* **14**, 609–612 (1910).
- [66] L. van Hove, *Phys. Rev.* **95**, 249–262 (1954).
- [67] P. Jund, W. Kob, and R. Jullien, *Phys. Rev. B* **64** (2001).
- [68] P. C. M. Fossati, L. Van Brutzel, A. Chartier, and J.-P. Crocombette, *Phys. Rev. B* **88**, 214112 (2013).
- [69] M. Born and K. Huang, *Dynamical theory of crystal lattices* (Oxford University Press, 1954) p. 420.
- [70] V. Sorkin, E. Polturak, and J. Adler, *Phys. Rev. B* **68**, 174102 (2003).
- [71] V. Sorkin, E. Polturak, and J. Adler, *Phys. Rev. B* **68**, 174103 (2003).
- [72] D. Wolf and S. Yip, *MRS Proc.* **230** (1991).
- [73] F. Guyot, P. Richet, P. Courtial, and P. Gillet, *Phys. Chem. Minerals* **20**, 141–146 (1993).
- [74] A. Stukowski, *Model. Simul. Mater. Sci. Eng.* **18**, 015012 (2010).